

# Multi-wavelength observations of the transitional millisecond pulsar binary XSS J12270-4859

D. de Martino<sup>1\*</sup>, A. Papitto<sup>2</sup>, T. Belloni<sup>3</sup>, M. Burgay<sup>4</sup>, E. De Ona Wilhelmi<sup>2</sup>, J. Li<sup>2</sup>, A. Pellizzoni<sup>4</sup>, A. Possenti<sup>4</sup>, N. Rea<sup>2,5</sup>, D.F. Torres<sup>2,6</sup>

<sup>1</sup> INAF – Osservatorio Astronomico di Capodimonte, Salita Moiariello 16, I-80131 Napoli, Italy

<sup>2</sup> Institut de Ciències de l’Espai (IEEC-CSIC), Campus UAB, c. Can Magrans s/n., E-08193 Barcelona, Spain

<sup>3</sup> INAF – Osservatorio Astronomico di Brera, Via E. Bianchi 46, I-23807 Merate (LC), Italy

<sup>4</sup> INAF – Osservatorio Astronomico di Cagliari, Via della Scienza, I-09047 Serlagius (CA), Italy

<sup>5</sup> Anton Pannekoek Institute, University of Amsterdam, Science Park 904, 1098XH Amsterdam, The Netherlands

<sup>6</sup> Institució Catalana de Recerca i Estudis Avançats (ICREA), E-08010, Barcelona, Spain

Accepted 2015 September 8. Received 2015 September 8; in original form 2015 July 10

## ABSTRACT

We present an analysis of X-ray, Ultraviolet and optical/near-IR photometric data of the transitional millisecond pulsar binary XSS J12270-4859, obtained at different epochs after the transition to a rotation-powered radio pulsar state. The observations, while confirming the large-amplitude orbital modulation found in previous studies after the state change, also reveal an energy dependence of the amplitudes as well as variations on time scale of months. The amplitude variations are anti-correlated in the X-ray and the UV/optical bands. The average X-ray spectrum is described by a power law with  $\Gamma$  index of 1.07(8) without requiring an additional thermal component. The power law index  $\Gamma$  varies from  $\sim 1.2$  to  $\sim 1.0$  between superior and inferior conjunction of the neutron star. We interpret the observed X-ray behaviour in terms of synchrotron radiation emitted in an extended intrabinary shock, located between the pulsar and the donor star, which is eclipsed due to the companion orbital motion. The G5 type donor dominates the UV/optical and near-IR emission and is similarly found to be heated up to  $\sim 6500$  K as in the disc state. The analysis of optical light curves gives a binary inclination  $46^\circ \lesssim i \lesssim 65^\circ$  and a mass ratio  $0.11 \lesssim q \lesssim 0.26$ . The donor mass is found to be  $0.15 \lesssim M_2 \lesssim 0.36 M_\odot$  for a neutron star mass of  $1.4 M_\odot$ . The variations in the amplitude of the orbital modulation are interpreted in terms of small changes in the mass flow rate from the donor star. The spectral energy distribution from radio to gamma-rays is composed by multiple contributions that are different from those observed during the accretion-powered state.

**Key words:** Interactive binaries – Stars: individual: XSS J12270-4859, 1FGL J1227.9-4852, 2FGL J1227.7-4853, 3FGL J1227.9-4854 – gamma-rays: stars- X-rays: binaries - Accretion

## 1 INTRODUCTION

Millisecond pulsars (MSPs) are believed to be formed in binary systems containing old neutron stars (NSs), which are spun-up to very short periods during a previous Gyr-long phase of mass accretion from an evolved companion. During this prolonged phase the binary appears as Low-Mass X-ray Binary (LMXB) and when mass accretion ceases a pulsar powered by the magnetic field rotation turns on and appears as a radio and gamma-ray pulsar. The MSP recycling scenario (Alpar et al. 1982) found observational support

through the discovery of first MS radio pulsar (Backer et al. 1982) and has dramatically been confirmed by the detection of few hundreds of galactic radio MSPs in binaries. Furthermore a few tens of accreting NSs spinning at a few ms are known (Patruno & Watts 2012), which are believed to be progenitors of MSP binaries. The transition between the two states was first testified by PSR J1023+0038, a (1.67ms) MSP found to be in an accretion disc-state between 2000–2001 (Archibald et al. 2009). This object was considered the "missing-link" between LMXBs and MSPs. It surprisingly turned on again in the X-ray band in 2013, showing X-ray pulsations at the NS spin period and disc emission lines in the optical band, thus testifying the presence of

\* E-mail: demartino@oacn.inaf.it

accretion at some level (Stappers et al. 2013; Takata et al. 2014; Patruno et al. 2014; Bogdanov et al. 2015). Another striking case is the one of IGR J1825-2452, a binary in the M28 globular cluster discovered as an accreting MSP during an outburst in 2013 (Papitto et al. 2013), but identified as a radio pulsar few years before (Bégin 2006). This source, turned into a radio pulsar at the end of the outburst, demonstrating that transitions between the accretion-powered and rotation-powered states can occur on timescales much shorter than secular evolution. The hard X-ray source XSS J12270-4859 (henceforth XSS J1227) was identified as an unusual low-luminosity ( $L_{0.3-10\text{keV}} \sim 6 \times 10^{33} \text{ erg s}^{-1}$  for a distance of 1.4 kpc) LMXB, surprisingly associated to a high energy gamma-ray *Fermi*-LAT source (de Martino et al. 2010, 2013; Hill et al. 2011, henceforth dM10,dM13). The peculiar X-ray and gamma-ray emission from this source was explained in terms of a system hosting a fast rotating NS in a propeller state (Papitto et al. 2014). In late 2012/beginning 2013 it faded to the lowest X-ray (Bogdanov et al. 2014) and optical (Bassa et al. 2014; de Martino et al. 2014, henceforth dM14) levels ever observed. Radio follow-ups revealed a fast (1.69 ms) rotating radio pulsar (Roy et al. 2015). Pulsed gamma-rays were also recently detected during the rotation-powered state (Johnson et al. 2015). X-ray pulses at the NS spin could then be detected in the previous disc-accretion state (Papitto et al. 2015), but not in the radio pulsar state because it is too faint. These three examples open the challenging possibility that during the evolution there is a phase where the NS "swings" back and forth from a radio pulsar to a sub-luminous ( $L_x \lesssim 10^{34} \text{ erg s}^{-1}$ ) disc accretion state. Analysing the spin period distribution of the accreting LMXBs, the radio MSPs and those undergoing Type-I bursts, Papitto et al. (2013) argued that nuclear MSPs are in an earlier evolutionary stage, while accreting MSPs are in a phase much closer to the switch-off and the turn-on of a radio MSP. Thus, the transitions between the two states may reflect the interplay between the NS magnetosphere and the mass transfer rate from the donor star (see Stella et al. 1994; Campana et al. 1998; Burderi et al. 2001). It is also argued that some, possibly most, of the so-called "redback" MSP binaries, which have non-degenerate donors, can display such state transitions (Roberts et al. 2015). Thus, all redbacks are potential "swinging" MSPs and searches for analogous sources are ongoing (e.g. Bogdanov & Halpern 2015).

The two known galactic field redbacks, PSR J1023+0038 and XSS J1227, linger in a sub-luminous disc accreting state since mid-2013 and in a radio pulsar state since end-2012, respectively. They represent ideal study cases to understand how transitions occur in redbacks. We here present the analysis of observations in the X-rays and UV band of XSS J1227 during the current rotation-powered state acquired with *XMM-Newton* in 2014 June and in the optical with the *REM* telescope in 2015 January and February aiming at studying the 6.91 h orbital variability of the source. We also compare the X-ray and UV/optical variability observed in 2013 December when it was first found to have transited to a disc-free state by Bogdanov et al. (2014), Bassa et al. (2014) and dM14. We further analyse the spectral energy distribution (SED) from radio to gamma-rays to identify the emission components in the radio pulsar state.

**Table 1.** Summary of the observations

Telescope	Instrument	UT Date	UT Start	$T_{\text{expo}}$ (ks)
<i>XMM-Newton</i>	EPIC-MOS1	2014-06-27	00:54:49	41.8
	EPIC-MOS2	2014-06-27	00:55:23	41.8
	OM-U	2014-06-27	01:03:50	42.5
Telescope	Instrument	UT Date	UT Start	$T_{\text{expo}}$ (sec)
<i>REM</i>	ROSS2	2015-01-20	02:46	300
		2015-01-21	02:40	300
		2015-01-23	02:32	300
		2015-02-12	01:16	300
		2015-02-13	01:24	300
		2015-02-14	01:10	300
	REMIR	2015-01-20	02:40	300*
		2015-01-21	02:40	300
		2015-01-23	02:24	300
		2015-02-12	01:20	300
		2015-02-13	01:10	300
		2015-02-14	01:44	300

\* 60s exposures in dithering mode at 5 positions

## 2 OBSERVATIONS

### 2.1 The *XMM-Newton* data

XSS J1227 was observed twice with *XMM-Newton* after the transition to the radio pulsar state which occurred between end 2012 and beginning 2013 (Bassa et al. 2014). The first observation, taken on Dec. 2013 December 29 (OBSID: 0727961401, hereafter Obs. 1), was analysed by Bogdanov et al. (2014). The second pointing was performed on 2014 June 27 (OBSID: 0729560801, hereafter Obs. 2) (see also Table 1). The former pointing used the EPIC-pn camera (Strüder et al. 2001) operated in Full Window Mode and with a thin optical blocking filter. In such a configuration the instrument retains a field of view of 25.6 x 26.2 arcmin, and has a temporal resolution of 73.4 ms. During Obs. 2 the EPIC-pn was instead set to the Timing fast mode to achieve a temporal resolution of 0.03 ms with the aim at detecting X-ray pulses at the 1.69 ms rotational period of the NS. In this observing mode 2-D imaging capabilities are lost. In both observations a Full Window observing mode with a thin filter was used for the two EPIC-MOS cameras (Turner et al. 2001), giving a time resolution of 2.6 s. Data were filtered to remove soft proton flares reducing the effective exposure to 34.6 and 41.8 ks in Obs. 1 and 2, respectively. As discussed in Papitto et al. (2015), the source is not detected in the EPIC-pn data obtained in Timing mode during Obs. 2. Therefore we focus only on the data acquired with the two EPIC MOS cameras and draw comparison between the two observations.

We analyzed data using the *XMM-Newton* Science Analysis Software (SAS) v.14.0<sup>1</sup>. EPIC MOS source photons were extracted from a 40 arcsec wide circle centered at the source

<sup>1</sup> <http://xmm.esac.esa.int/sas/>

position, to encircle  $\approx 85\%$  of the source photons. Background was accumulated from a 50 arcsec wide circular region far from the source. X-ray photons were reported to the Solar system barycentre using the optical position of the source reported by (Masetti et al. 2006). XSS J1227 was detected by each MOS camera at an average net level of  $0.025(8)$  cts s $^{-1}$  and of  $0.040(9)$  cts s $^{-1}$  in Obs. 1 and 2, respectively.

In Obs. 1 and 2, the Optical Monitor (OM) (Mason et al. 2001) was operated in Fast mode, giving a temporal resolution of 0.5 s, with the U filter (3500–4800 Å). Ten exposures were acquired in both observations for a total of 32.7 ks (Obs. 1) and 42.5 ks (Obs. 2). The OM-U band data of Obs. 1 were presented in Bassa et al. (2014). For a comparative analysis of the two observations, the two data sets were reprocessed and photometry was extracted using the SAS task *omchain*. In a few exposures during Obs. 2 the source was not detected and photometry was extracted performing manual detection of the target using the *omsource* task. The source was at an average magnitude of  $U=19.43(3)$  and  $19.92(4)$  in Obs. 1 and 2, respectively. Correction to the Solar system barycentre was also applied.

## 2.2 The REM photometric data

XSS J1227 was observed from 2015 Jan. 20 to Jan. 23 (hereafter Run 1) and from 2015 Feb. 12 to Feb. 14 (hereafter Run 2) with the 0.6m INAF *REM* telescope in La Silla, Chile (Zerbi et al. 2004). The telescope is equipped with the ROSS2 camera<sup>2</sup> that performs simultaneous exposures in the Sloan filters  $g'$ ,  $r'$ ,  $i'$  and  $z'$  and with the REMIR camera (Conconi et al. 2004) covering simultaneously the near-IR in one band. Integration times were 300 s for all optical filters and a dithering of 5 exposures of 60 s was used for the REMIR J-band exposures. The night of Jan. 22 was not photometric and thus the data are not included here. The total coverages were 3.2 h, 3.51 h and 4.1 h in Run 1 and 4.6 h 5.3 h 5.5 h in Run 2. The log of the photometric observations is also reported in Table 1.

The photometric data sets were reduced using standard routines of IRAF to perform bias and flat-field corrections. Due to the low response of the  $z'$  filter the corresponding images have not been analysed. For the REMIR observations the five dithered images were merged into a single frame.

For each data set, aperture photometry was performed optimizing aperture radius and sky subtraction was done using annuli of different sizes. Comparison stars were used to check and to correct for variable sky conditions. The *REM/ROSS2* and REMIR photometry was calibrated using the Sloan standard SA 94 242 observed each night whose near-IR magnitudes are also tabulated in the 2MASS catalogue<sup>3</sup>. XSS J1227 was found at  $g'=18.62(2)$ ,  $r'=18.12(4)$ ,  $i'=17.96(2)$  in Run 1 and at  $g'=18.75(3)$ ,  $r'=18.28(3)$  and  $i'=17.91(4)$  in Run 2. Because the source was barely detected in the individual J band images, image coaddition for each night was performed to provide a mean magnitude. XSS J1227 was at  $J=16.98(4)$  and  $J=16.92(4)$  in Run 1 and

<sup>2</sup> <http://www.rem.inaf.it>

<sup>3</sup> <http://www.ipac.caltech.edu/2mass/>

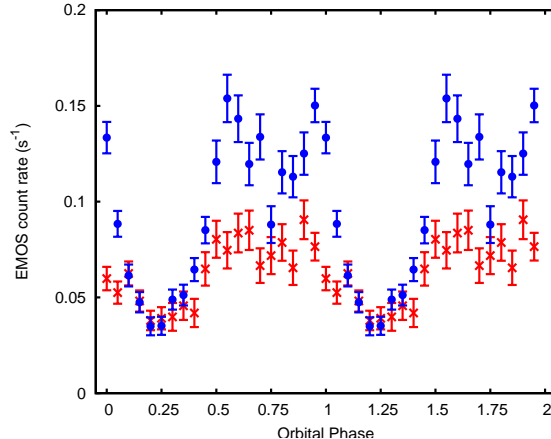


**Figure 1.** X-ray orbital modulation observed during Obs. 1 (red crosses) and Obs. 2 (blue circles), evaluated in 20 phase bins by folding the background subtracted summed light curves observed by the two MOS cameras in the 0.3–10 keV band, at the 6.91 h orbital period according to the radio pulsar ephemeris given in Papitto et al. (2015). Phase 0 corresponds to the passage of the NS at the ascending node of the orbit.

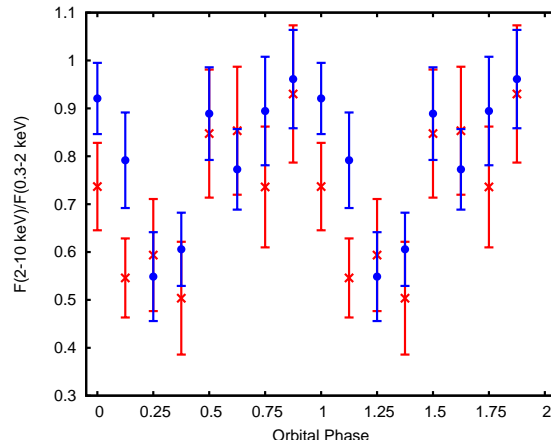


**Figure 2.** Orbital modulation of the hardness ratio evaluated as the ratio of fluxes in the 2–10 keV and 0.3–2 keV bands in 8 phase bins (see Fig. 1).

2, respectively. The  $g'$ ,  $r'$  and  $i'$  light curves were also corrected to the Solar system barycentre.

## 3 RESULTS

### 3.1 The X-ray orbital variability

The background subtracted summed MOS light curves in the 0.3–10 keV range during Obs. 1 and 2 were folded at the orbital period using the radio pulsar ephemeris given by Papitto et al. (2015) where phase 0 is defined as the epoch at which the NS passes at the ascending node of the orbit. The uncertainties on the determination of the orbital phase with these ephemeris is  $\lesssim 1\%$  for the two epochs. The orbital modulation observed in Obs. 1 and 2 binned in 20 phase intervals, each lasting  $\simeq 1.25$  ks is plotted in Fig. 1. A minimum count-rate of  $0.04$  cts s $^{-1}$  is observed in both observations at orbital phase  $\phi = 0.25$ , i.e. when the donor

star is between the pulsar and the observer. The intensity then increases when the pulsar approaches the closest distance to the observer ( $\phi = 0.75$ ). However, during Obs. 2 the increase of the flux is steeper and the flux at maximum roughly doubles that during Obs. 1. The modulation amplitude, defined as  $(F_{\max} - F_{\min})/(F_{\max} + F_{\min})$ , evaluated with a simple sinusoidal function is 0.25(4) and 0.69(6). Also, a dip is observed during Obs. 2 centred at  $\phi = 0.75$  where the count rate decreases by a factor  $\sim 2$ . This dip is instead marginally visible in Obs. 1.

An orbital variability is also displayed by the hardness ratio evaluated as the ratio of the flux observed in the 2-10 keV band to the flux in the 0.3-2 keV band (see Fig. 2). The orbital modulation was sampled using 8 phase bins in order to increase the counting statistics of each point. In both observations, the hardness ratio increases by a factor  $\sim 1.5$  at maximum of the modulation, implying that the spectrum gets harder when the pulsar is at inferior conjunction. The significance of the orbital variability of the hardness ratio is higher in Obs. 2 than in Obs. 1. Modelling the orbital profile of the hardness ratio (in Fig. 2) with a constant gives  $\chi^2_r = 1.76$  and  $\chi^2_r = 2.8$  for 7 d.o.f. in Obs. 1 and Obs. 2, respectively. This gives a probability that the profiles are compatible with a constant of 0.091 and 0.005, respectively. The significance of a detection of the orbital variability in the hardness ratio is therefore 1.7 and  $2.8\sigma$  in Obs. 1 and Obs. 2. In both cases, a sinusoidal fit to the orbital profile yields an improvement of the modelling with respect to a constant, which has a probability of  $\sim 5\%$  of being due to statistical fluctuations (F-test). We also note that the source is significantly detected in all orbital phase bins in the two energy bands at a significance larger than  $10\sigma$ .

### 3.2 The X-ray spectrum

For each epoch, the spectra from the two MOS cameras in the range 0.3-10 keV were fitted together using the same spectral parameters. During Obs. 2 the spectrum is well described ( $\chi^2_r = 1.18$  for 123 d.o.f.) by a power law with index  $\Gamma = 1.07 \pm 0.08$  (all uncertainties on the spectral parameters are quoted at the 90% confidence level). Only an upper limit of  $N_H < 5 \times 10^{20} \text{ cm}^{-2}$  (90% confidence level) could be set on the absorption column. The 0.3-10 keV average unabsorbed flux is  $7.1 \pm 0.4 \times 10^{-13} \text{ erg cm}^{-2} \text{ s}^{-1}$ . The addition of a thermal component, either a blackbody (BBODYRAD model in XSpec) or a more physical NS atmosphere (NSA model in XSpec, (Zavlin 2006)), does not give an improvement of the modelling. Fixing in NSA the NS mass and radius to  $1.4 M_\odot$  and 10 km, and using the low field option  $B=0 \text{ G}$ , we obtain an upper limit on the 0.3-10 keV flux of such a thermal component of  $2 \times 10^{-14} \text{ erg cm}^{-2} \text{ s}^{-1}$ , i.e.  $\simeq 3\%$  of the total flux.

We also modelled the spectra during Obs. 2 at orbital phases close to the NS superior conjunction ( $\phi$  ranging between 0.1 and 0.4), and to the NS inferior conjunction ( $\phi$  ranging between 0.5 and 1.0). As indicated by the hardness ratio, close to the orbital minimum the spectrum gets softer and can be described by a power law with index  $\Gamma = 1.30^{+0.25}_{-0.15}$  ( $\chi^2_r = 1.03$  for 21 d.o.f.). The 0.3-10 keV unabsorbed flux is  $2.8 \pm 0.4 \times 10^{-13} \text{ erg cm}^{-2} \text{ s}^{-1}$ . A thermal NS atmosphere component is not statistically required to model the spectrum, and would contribute to at most to 40% of the flux in

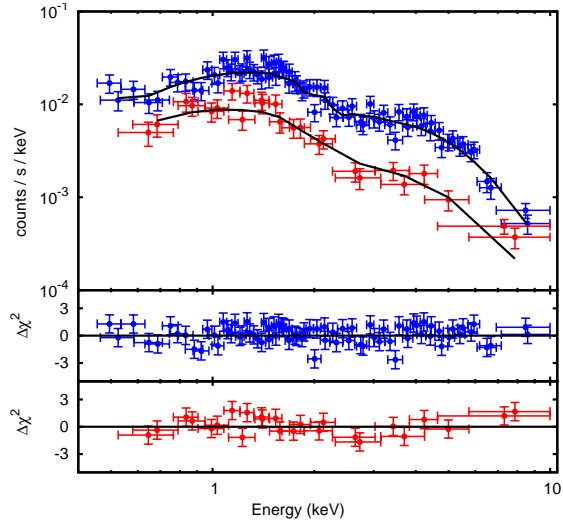


**Figure 3.** The phase-resolved MOS spectra during Obs. 2 (top panel) at orbital phases close to the NS inferior conjunction ( $\phi = 0.5 - 1.0$ , blue points) and close to the NS superior conjunction ( $\phi = 0.1 - 0.4$ , red points). Middle and bottom panels show residuals with the best fit absorbed power law model, shown as a black solid line.

the same energy range ( $1.1^{+0.9}_{-0.4} \times 10^{-13} \text{ erg cm}^{-2} \text{ s}^{-1}$ ). Close to the NS inferior conjunction the spectrum is described by a harder ( $\Gamma = 1.0 \pm 0.1$ ) power law ( $\chi^2_r = 0.93$  for 73 d.o.f.) that emits a 0.3-10 keV flux of  $1.08 \pm 0.08 \times 10^{-12} \text{ erg cm}^{-2} \text{ s}^{-1}$ . In this case, a thermal component would contribute to at most 13% of the total flux. The fits to the MOS spectra and those at the two phases using the simple absorbed power law are shown in Fig. 3.

The fit to the MOS spectra during Obs. 1 is consistent with the results found by Bogdanov et al. (2014) for the EPIC-pn spectrum, the power law index being  $\Gamma = 1.2 \pm 0.1$  ( $\chi^2_r = 0.87$  for 79 d.o.f.) and an upper limit to the hydrogen column density  $N_H < 6.8 \times 10^{20} \text{ cm}^{-2}$  (90% confidence level). The unabsorbed flux in the 0.3-10 keV range is  $4.4 \pm 0.1 \times 10^{-13} \text{ erg cm}^{-2} \text{ s}^{-1}$ . Due to the lower sensitivity of the MOS cameras with respect to the EPIC-pn, we are unable to conclude on the detection of the NS thermal emission. Here we note that the spectral fits to the EPIC-pn data do not improve but not exclude a thermal component (Bogdanov et al. 2014).

Comparing the power law indexes during the previous disc-accretion state (dM10,dM13) ( $\Gamma = 1.7$ ) the spectra are harder during the disc-free states in Obs. 1 and 2 and the absorption contribution is consistent with that previously determined in dM10 and dM13. The luminosity in the 0.3-10 keV range, assuming  $d=1.4 \text{ kpc}$  as derived from the radio DM measures (Roy et al. 2015), results to be  $1.0-1.7 \times 10^{32} \text{ erg s}^{-1}$  at the two epochs, one order of magnitude lower than in the disc-accretion state.

### 3.3 The UV/optical orbital modulation

We folded the UV photometric data of Obs. 1 and 2 at the orbital period using the same ephemeris adopted for the X-ray band. The orbital modulation in the UV band at the two epochs is reported in Fig. 4. The UV flux is minimum

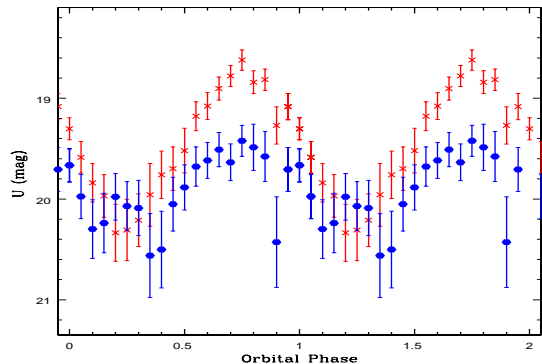


**Figure 4.** Orbital modulation observed in the OM U band during Obs. 1 (red crosses) and Obs. 2 (blue circles), evaluated in 20 phase bins.

at  $\phi \sim 0.25$  when the source shows roughly the same magnitude ( $U \sim 20.4$ ) in both observations. The UV flux reaches a maximum at  $\phi \sim 0.75$  where it increases by 1.43(4) mag and by 0.72(9) mag in Obs. 1 and 2, respectively. The slight decrease at  $\phi \sim 0.9$  in Obs. 2 is not significant from inspection of the unfolded light curve. The UV and X-ray band modulations are thus in phase, but the amplitudes in the two bands behave in opposite way. In Obs. 1 the X-ray amplitudes are larger than in Obs. 2, but the UV amplitudes are lower in Obs. 1 than in Obs. 2 (see Fig. 1).

We folded the optical g', r' and i' REM photometry of 2015 Jan. (Run 1) and Feb. (Run 2) at the orbital period using the same ephemeris. In Fig. 5 we report the orbital modulation observed at the two epochs together with the g'-i' colour index. Likewise the X-ray and U bands, the modulations in the optical/near-IR bands show a minimum centred at  $\phi=0.25$  and a maximum at  $\phi=0.75$ . As evaluated with sinusoidal fits the modulation amplitude is  $\Delta g'=0.84(2)$  mag,  $\Delta r'=0.74(1)$  mag and  $\Delta i'=0.56(1)$  mag in Run 1, and it is  $\Delta g'=0.72(2)$  mag,  $\Delta r'=0.52(1)$  mag and  $\Delta i'=0.40(1)$  mag in Run 2. The source is also on average brighter in g' and r' by 0.1 mag in Run 1 than in Run 2. A comparison with the optical level observed in 2013 Dec. (dM14), the source was at about the same g' magnitude as in Run 2, with a modulation of similar amplitude. The modulation is also colour dependent and exemplified by the g'-i' index (bottom panels of Fig. 5), indicating a reddening at orbital minimum when the donor star is at inferior conjunction. The average values are  $g'-i'=0.66(6)$  and  $g'-i'=0.84(4)$  in Run 1 and 2, respectively. The source thus appears redder when on average fainter.

The large amplitude modulation and strong colour variability confirm the previous finding that the donor star suffers irradiation (dM14). Similarly, we applied the NIGHTFALL code<sup>4</sup> to fit simultaneously the g', r' and i' light curves with the aid of the donor star radial velocity curve presented in dM14. We adopted a blackbody temperature of 5000 K as starting point for the unheated star and fixed the maximum allowed temperature (500 000 K) for the irradiating star treated as a point source. The donor star is assumed to fill its Roche lobe which is consistent with the occurrence

of radio eclipses for  $\sim 40\%$  of the orbit (Roy et al. 2015). We left the mass ratio  $q$ , the binary inclination  $i$  and the donor star temperature  $T_2$  free to vary. We derive for Run 1  $q = 0.09 \pm 0.08$ ,  $i = 53^{+10}_{-13}^\circ$  and  $T_2 = 6000 \pm 500$  K heated up to 6500 K ( $\chi^2_r = 9.5$  for 362 d.o.f.) (uncertainties are at  $1\sigma$  confidence level) and for Run 2  $q = 0.19^{+0.15}_{-0.19}$ ,  $i = 50^{+20}_{-10}^\circ$  and  $T_2 = 5900 \pm 400$  K heated up to 6300 K ( $\chi^2_r = 15.3$  for 482 d.o.f.). The large  $\chi^2_r$  are due to the small errorbars of the photometric measures. The g', r' and i' light curves show asymmetries in the portion rising to the maximum but the inclusion of cold or hot spots (Romani et al. 2012) does not improve the fits. Similar behaviour is also found in the black widow binary PSR J1311-3438 by Romani et al. (2015), suggesting that the donor face is not fully heated by a point source and that the asymmetric shock may provide at least some of the heating. We also used the U band photometry of Obs. 1 together with the donor star radial velocities and find  $q = 0.16^{+0.10}_{-0.05}$ ,  $i = 58^{+7}_{-12}^\circ$  and  $T_2 = 5500 \pm 300$  K heated up to 6000 K ( $\chi^2_r = 6.2$  for 88 d.o.f.). The addition of the g' and r' photometry acquired in dec. 2013 (dM14) does not improve the results because of the large scatter and the sparse orbital coverage of the data. In all three data sets the mass ratio  $q$  is consistent within errors with that derived from radio data by Roy et al. (2015),  $q=0.194(3)$ . We note that the large filling factor of the donor implies an aspherical shape for the star that causes strong temperature (brightness) variations over the surface and the model code provides a mean temperature of the heated face of the secondary. The g', r', i' fluxes at the peak of the modulation observed in Run 1 and 2, when dereddened for intervening absorption  $E_{B-V} = 0.11$  (dM10), are consistent with a blackbody with temperatures similar to those derived from the light curve models,  $6600 \pm 200$  K and  $6300 \pm 300$  K, respectively. The blackbody normalisation decreases by a factor of  $1.17 \pm 0.01$  between Run 1 and 2. We therefore confirm the findings in dM14, that the donor star temperature is compatible with that of a G5 star seen at inferior conjunction and it reflects a F5 spectral type at superior conjunction. Since the binary parameters  $q$  and  $i$  cannot explain the variability in the amplitudes observed at the different epochs, we also conclude that the variations are due to changes in the visible area of the irradiated face of the donor star (see also Sect. 4). In the following we will assume  $0.11 \lesssim q \lesssim 0.26$  and  $46^\circ \lesssim i \lesssim 65^\circ$ . For a NS mass of  $1.4 M_\odot$ , the mass ratio gives a mass of donor star  $0.15 \lesssim M_2 \lesssim 0.36$ .

## 4 DISCUSSION

We here discuss the X-ray and UV/optical orbital variability of XSS J1227 during the current disc-free state.

### 4.1 The X-ray and optical variabilities

The X-ray flux is strongly modulated and it is maximum close to the inferior conjunction of the NS. The minimum occurs at the same phases of the radio eclipses (Roy et al. 2015), which are produced by the orbital motion of the secondary star. X-ray orbital modulations are also observed in other redbacks (Roberts et al. 2015). The X-ray spectrum as well as those at minimum and maximum of the modulation

<sup>4</sup> The NIGHTFALL code is available at <http://www.hs.uni-hamburg.de/DE/Ins/Per/Wichmann/Nightfall.html>

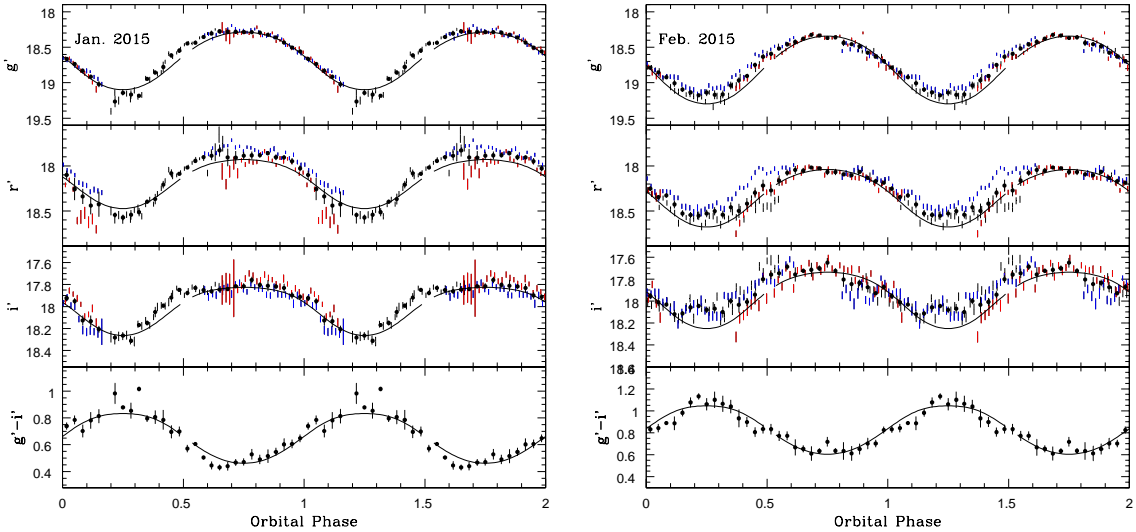


**Figure 5.** From top to bottom: The orbital modulation in the optical  $g'$ ,  $r'$  and  $i'$  bands and the  $g'-i'$  index as observed in Run 1 (left) and Run 2 (right). Single nights are reported with points of different colours and the average of the three nights as black points evaluated in 30 phase bins. The black lines report the best fit NIGHTFALL curves (see text for details).

suggest that the X-ray emission originates in an intrabinary shock produced by the interaction of the outflow from the donor star and the wind from the pulsar (Arons & Tavani 1993) and/or in the pulsar magnetosphere (Possenti et al. 2002). The long duration of the X-ray eclipse,  $\sim 30\%$  of the orbital cycle, suggests that the X-ray emission is extended and originates close to the donor star and presumably at the L1 point, supporting an origin in the intrabinary shock. Similar interpretation is given for other eclipsing redbacks (Bogdanov et al. 2011; Li et al. 2014), where the X-ray modulation is caused by the eclipse of the intrabinary shock emission by the donor. The eclipse depth and duration depend on the ratio between the donor star radius and the intrabinary shock separation and on the binary inclination. The shock location or apex is defined as  $r_s/a \sim 1/(1 + \eta^{1/2})$  (Arons & Tavani 1993), where  $a$  is the binary separation and  $\eta \sim \dot{M} v_w c / L_{sd}$  is the momentum ratio between the stellar wind and the pulsar wind. Unfortunately, this quantity cannot be determined because the mass loss rate during the radio pulsar state is unknown and thus also the shock apex. For what follows we assume  $r_s \sim R_{L,NS} \sim 1.1 - 1.2 \times 10^{11}$  cm adopting the mass of the components in Sect. 3.3. For an isotropic pulsar wind the geometric fraction of the wind stopped by the shock, assumed to be of the same size of the Roche-lobe filling donor star, is  $f_s \sim 0.5(1 - \cos \Omega) \sim 0.02$ , where  $\Omega = \text{atan}(R_2/R_{L,NS})$  and  $R_2 = R_{L2} = 0.462(q/1+q)^{1/3} a \sim 3.2 - 4.2 \times 10^{10}$  cm for the range of  $q$  found in Sect. 3.3. This fraction is similar to those inferred in other redbacks (Roberts et al. 2015).

The shock is expected to emit synchrotron radiation. To estimate the synchrotron luminosity from the shock we follow Arons & Tavani (1993) and Kennel & Coroniti (1984). Similar arguments were also used by Stappers et al. (2003) for the black widow binary PSR B1957+20 and first invoked for the redback binary PSR J0024-7204W in the globular cluster 47 Tuc by Bogdanov et al. (2005) and later also for PSR J1023+0038 by Bogdanov et al. (2011). The

X-ray luminosity emitted by the shock depends on both the post-shock magnetic field strength and the ratio of magnetic and particle energy density  $\sigma$ . This fraction is not known but could be as low as  $\sigma=0.003$  in winds dominated by kinetic energy, like the Crab pulsar, or as high as  $\sigma >> 1$  for strongly magnetised winds (Stappers et al. 2003). Given the small separation between the pulsar and the companion, the intrabinary shock is expected to be located in a strong magnetic field (Arons & Tavani 1993; Stappers et al. 2003). The magnetic field upstream of the shock is  $B_1 = [(\sigma/(1+\sigma)(\dot{E}/c f_p r^2)]^{1/2}$ , where  $f_p$  is the pulsar isotropic factor and  $\dot{E}$  is the spin-down energy of the pulsar. In the two extreme cases, assuming a pulsar energy loss of  $\dot{E} \sim 9 \times 10^{34}$  erg s $^{-1}$  (Roy et al. 2015), an isotropic wind  $f_p=1$  and the shock at  $r_s \sim R_{L,NS} \sim 1.2 \times 10^{11}$  cm, we obtain  $B_1 \sim 0.8$  G and  $\sim 16$  G, respectively. The post-shock magnetic field is  $B_2 \sim 3B_1 \sim 2.5$  G for  $\sigma \ll 0.01$  and it is  $B_2 \sim B_1 \sim 16$  G for high- $\sigma$  values (Kennel & Coroniti 1984). For simplicity we assume that the observed X-ray luminosity totally originates via synchrotron emission from the shock. This requires that the electrons are relativistic with  $\gamma \sim 2.5 \times 10^5 (\epsilon/B_2)^{1/2}$ , where  $\epsilon$  is the observed photon energy,  $\sim 10$  keV. Thus  $\gamma \sim 2 - 5 \times 10^5$  in the case of magnetic and kinetic energy dominated winds, respectively. The expected synchrotron luminosity is  $L_{\text{sync}} \sim f_{\text{sync}} f_\gamma f_s L_{sd}$ , where  $L_{sd}$  is the spin-down luminosity,  $f_\gamma$  is the fraction of spin down energy flux that accelerates electrons with Lorentz factor  $\gamma$  at 10 keV, and  $f_{\text{sync}} = (1 + t_{\text{sync}}/t_{\text{flow}})^{-1}$  is the radiative efficiency of the synchrotron emission. Here  $t_{\text{sync}}$  is the radiative synchrotron loss time and  $t_{\text{flow}}$  is the time of residence of particles radiating in the shock. For the assumed shock size of the order of the donor star diameter  $t_{\text{flow}} \sim (3r/c) \sim 6-9$  s for  $\sigma \ll 1$  and  $t_{\text{flow}} \sim (r/c) \sim 2-3$  s for high- $\sigma$  flows (Kennel & Coroniti 1984). The radiative loss time  $t_{\text{sync}} = 5 \times 10^8 / (\gamma B_2^2)$  is  $\sim 10$  s and  $\sim 160$  s for  $\sigma >> 1$  and  $\sigma \ll 1$ , respectively. Thus  $f_{\text{sync}} \sim 0.04 - 0.05$  for kinetic dominated winds and  $f_{\text{sync}} \sim 0.17 - 0.23$  for mag-

netic dominated winds. Using the geometric factor  $f_s \sim 0.02$  derived above and the observed 0.3-10 keV X-ray luminosity at orbital maximum of  $2.5 \times 10^{32} \text{ erg s}^{-1}$ , we obtain  $f_\gamma \sim 0.60 - 0.81$  for the highly magnetic case and unphysical values  $f_\gamma \sim 3$  for the kinetic dominated wind case. These large values reflect the geometrical uncertainties of the pulsar wind  $f_p$  and the fraction stopped by the shock  $f_s$ , indicating that the pulsar wind is not isotropic and hence the  $f_s \gtrsim 0.02$  should be regarded as a lower limit. The unphysical values for  $f_\gamma$  in the low- $\sigma$  limit also imply that the wind must be magnetically dominated. Similar conclusions were drawn for PSR J1023+0038 (Bogdanov et al. 2011).

The X-ray spectrum hardens at orbital maximum with  $\Gamma \sim 1.0$ , whilst at minimum  $\Gamma \sim 1.3$ . A hardening at orbital maximum is a new observational aspect in redbacks, as it has been only detected in PSR J2129-0429 (Hui et al. 2015) so far. It is instead observed in other more massive gamma-ray binaries such as LS 5039 (Li et al. 2011). The hardening cannot be due to photoelectric absorption since it would occur at orbital minimum. It could suggest the presence of an additional contribution to the X-ray emission. In spin-powered X-ray pulsars, a fraction  $\sim 10^{-4}$  of the spin down luminosity is converted in X-rays. Using the empirical relation by Possenti et al. (2002), for  $L_{\text{sd}} \sim 9 \times 10^{34} \text{ erg s}^{-1}$  an X-ray luminosity of magnetospheric origin  $\sim 3.5 \times 10^{31} \text{ erg s}^{-1}$  is expected in the 2-10 keV range. This is not much different from that observed at minimum in the same energy range:  $L_{X,\text{min}} \sim 4.9 \times 10^{31} \text{ erg s}^{-1}$ . This emission should be pulsed at the spin period of the NS. Unfortunately the source is not detected in the EPIC-pn timing data during Obs. 2, but Papitto et al. (2015) derive an upper limit on the 0.5-10 keV pulsed luminosity of  $\sim 1.6 \times 10^{31} \text{ erg s}^{-1}$ . The limit on the NS thermal emission at minimum is estimated as  $\sim 0.4 L_{X,\text{min}} \sim 2.5 \times 10^{31} \text{ erg s}^{-1}$  in the 0.3-10 keV range (sect. 3.2). Furthermore, at X-ray orbital minimum the shock could still contribute, because of its large size and the energy distribution of the electron population may be softer in the outer shock regions. Therefore, it is not possible to conclude whether the observed softening at orbital minimum is due to the extended shock, to the NS or both. Furthermore while only a hint of a dip superposed on the broad maximum could be detected in Obs. 1, this feature is observed when source is brighter in Obs. 2 (see Fig. 1). A double-peaked maximum is also present in PSR J2129-0429 (Hui et al. 2015; Roberts et al. 2015) at similar orbital phases. In PSR J1023+0038 an enhancement of emission is observed at eclipse egress (Bogdanov et al. 2011). These variations are interpreted as due to Doppler boosting due to the finite velocity of the shock wind in the direction of the post-shock flow (Arons & Tavani 1993; Stappers et al. 2003; Bogdanov et al. 2011; Huang et al. 2012). If the shock wraps the donor star, the plasma accelerates as it flows around the companion and, around inferior conjunction of the donor star, the electrons are accelerated primarily in the direction of the observer. At this phase an increase of flux would be expected, but due to obscuration by the donor star, the enhancements would occur before and after the eclipse. For PSR J1023+0038 the absence of enhancement prior the eclipse ingress was interpreted as due to a weaker outflow toward the leading edge of the eclipse (Bogdanov et al. 2011). For post-shock velocities in the range  $c/3 - c/3^{1/2}$ , Arons & Tavani (1993) predict brightness variations by a

factor of  $\sim 1.3\text{-}2.2$ , respectively. The flux variations at the dip of a factor  $\sim 2$  observed in Obs. 2 is consistent with this prediction.

In Obs. 2 the X-ray peak flux at maximum is  $\sim 2$  times larger than on Obs. 1. If the mass loss rate and thus the luminosity increases, then the momentum ratio  $\eta$  increases and the shock apex moves inward the NS Roche lobe. However, a change by a factor of  $\sim 2$  in the mass loss rate will marginally affect the apex radius, but it may produce an increase in size of the shock. This would imply an increase of the time of residence of electrons  $t_{\text{flow}}$  in the shock and of the fraction of the pulsar wind intercepted by the shock ( $f_s$ ). It could be also possible that the relativistic plasma accelerating as it flows around the companion may reach larger velocities giving rise a larger Doppler boosting effect as observed in Obs. 2.

The orbital modulation in the UV/optical is strong, amounting to  $\sim 0.7\text{-}0.8$  mag in the optical and up to  $\sim 1.4$  mag in the UV. The optical colours along the orbital cycle indicate a reddening at inferior conjunction of the donor star. The light curves are well described a G5 type donor star filling its Roche lobe and heated up to  $\sim 6500$  K, although the modelling considers a point-like irradiating source at the NS and not at L1. Thus the donor star is heated by high energy radiation from either the shock and/or by the pulsar wind. We here recall that irradiation of the secondary was also found to occur before the state transition (dM14). As also noted in dM14, the donor is not expected to substantially cool, because the thermal relaxation time scale is of the order of the Kelvin-Helmholtz time of the convective envelope,  $\tau_{\text{KH}} \sim (M_2^2/R_2 L_2)$ . The observed changes in the amplitudes of the UV/optical orbital modulation would then be due to changes of the visible area of the heated face of the companion rather than to temperature variations. Thus, the opposite behaviour seen in the X-ray and UV modulation amplitudes could be explained in terms of a larger size of the shock, producing a stronger X-ray modulation, and at the same time preventing the irradiated face to be totally visible, yielding to a weaker modulation in the UV and optical bands. The heating effect on the donor star,  $L_{\text{irr}} = 4\pi R_2^2 \sigma T_{\text{irr}}^4 \sim 1.2 - 2.2 \times 10^{33} \text{ erg s}^{-1}$  for  $T_{\text{irr}} \sim 6500$  K<sup>5</sup>, is larger than that estimated for the shock  $\sim 3 \times 10^{32} \text{ erg s}^{-1}$  in the 0.3-10 keV range. However, if the X-ray spectrum extends well beyond 10 keV, as observed by *NuSTAR* in PSR J1023+0038 with no spectral break up to 79 keV (Tendulkar et al. 2014), the X-ray luminosity at orbital maximum in the 0.3-100 keV range can be about one order of magnitude higher than that measured in the *XMM-Newton* EPIC range. In this case the shock could be totally responsible for the heating of the donor star. If instead we consider the pulsar spin-down power, we infer that  $\sim 0.45$  of the spin-down luminosity goes into the heating of the donor star. Observations at higher energies will clarify this issue.

<sup>5</sup> A detailed and rigorous treatment of the irradiation of the donor star can be found in Ritter et al. (2000). The effect of irradiation is to suppress the temperature gradient in the outer stellar envelope and blocking the outward transport of energy through the face. Thus the emergent flux from the irradiated face is:  $F_{\text{irr}} = \sigma T_{\text{irr}}^4 = W F_{\text{inc}}$ , with  $W \sim 0.5$ , the albedo for a star in convective equilibrium.

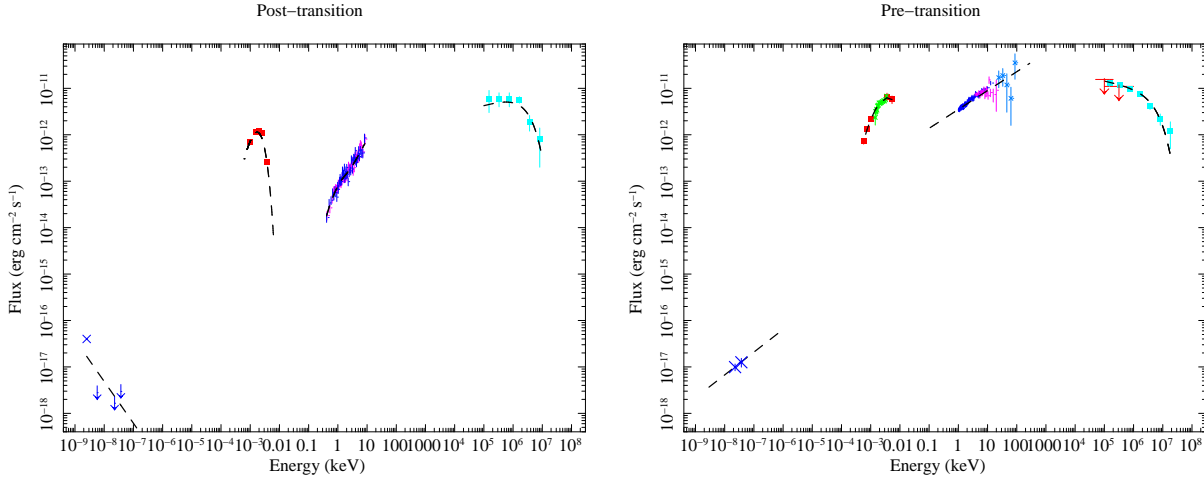


**Figure 6.** The broad-band spectral energy distributions (SED) of XSS J1227 during the rotation-powered state (left panel) and during the sub-luminous pre-transition state (right panel). The post-transition SED is constructed with the X-ray spectra of the two MOS cameras (blue and magenta), the UV OM and optical REM photometry (red squares), the radio measures reported by Roy et al. (2015) (blue crosses) and the upper limit by Bassa et al. (2014) (blue arrows) and the *Fermi*-LAT (light blue) fluxes reported in Xing & Wang (2014) together with the corresponding fitted model (see text for details). The pre-transition SED is taken from dM13 but substituting the *Fermi*-LAT fluxes reported in the second release catalogue with those in Xing & Wang (2014) together with the corresponding model fit.

#### 4.2 The spectral energy distribution

We constructed a broad-band spectral energy distribution (SED) from radio to gamma-rays during the rotation-powered state, shown in the left panel of Fig.6. We used the radio flux at 607 MHz as measured by Roy et al. (2015) and the upper limits obtained at 1.4, 5.5 and 9 GHz reported by Bassa et al. (2014). These are broadly consistent with the spectral slope expected from a radio pulsar with a power law index -1.7 (Roy et al. 2015). For the UV/optical range we use the average U and g', r', i' and J band magnitudes obtained in 2014 and 2015 respectively, corrected for intervening absorption  $E_{B-V} = 0.11$  (dM10) and overlay the best fit blackbody model with  $T_{bb} = 5200 \pm 300$  K. The unabsorbed average X-ray spectra in the 0.3–10 keV range of the two MOS cameras during Obs 2 are reported together with the best fit power law with  $\Gamma=1.07$ . We also add the *Fermi*-LAT spectrum after the state transition from Xing & Wang (2014), together with a power law with an exponential cut-off with index  $\Gamma=1.8$  and energy cutoff  $E_c = 2$  GeV obtained by the same authors. Here we note that also Johnson et al. (2015) analyse the *Fermi*-LAT data obtaining comparable values. In the right panel of Fig.6 we also report the SED obtained during the previous LMXB state presented in dM13, substituting the *Fermi*-LAT fluxes, obtained at that time from the second release of the source catalogue (2FGL), with those reported by Xing & Wang (2014) during the same pre-transition state together with their best fit power law exponential cut-off with index  $\Gamma=2.13$  and  $E_c = 6$  GeV. Also in this case the fit parameters are compatible within uncertainties with those recently obtained by Johnson et al. (2015) analysing the same period.

The SEDs at the two epochs substantially differ from each other implying very different contributions. In the post-transition state, the radio flux is a factor  $\sim 6$  lower than that observed in the disc state and the slope is consistent with that of a radio pulsar (Roy et al. 2014). The

UV/optical/near-IR emission totally originates from the donor star, whilst an additional contribution from the disc is required in the LMXB state (dM14). The X-ray emission in the radio pulsar state is harder than that before the transition ( $\Gamma \sim 1.7$ , dM13). In the LMXB state the X-ray and gamma-ray emissions have been successfully modelled by a propeller scenario (Papitto et al. 2014; Papitto & Torres 2015) with marginal accretion from the NS, while in the rotation-powered state the X-ray emission mainly originates from the intrabinary shock. The post-transition gamma-ray emission appears instead to originate in the pulsar outer magnetosphere (Johnson et al. 2015) from the observed partially alignment of the *Fermi*-LAT and radio spin light curves and the lack of an orbital modulation at GeV energies<sup>6</sup>. The gamma-ray luminosity was found by Johnson et al. (2015) to be  $\sim 5\%$  of the pulsar spin-down energy. Although the lack of X-ray coverage extending above 10 keV cannot allow us to draw conclusions, the present data suggest that the X-rays and high energy gamma-rays are not linked.

#### 5 CONCLUSIONS

We have analysed the X-ray and optical emissions of XSS J1227 during the ongoing rotation-powered state into which the source entered at the end of 2012/beginning 2013. We here summarize the main results:

- The X-ray luminosity in the 0.3–10 keV range during the radio pulsar state is  $\sim 1.0 - 1.7 \times 10^{32}$  erg s<sup>-1</sup>, one order of magnitude lower than that in the previous accretion-

<sup>6</sup> The claim of a weak orbital modulation by Xing & Wang (2014) during the rotation-powered state is not confirmed by Johnson et al. (2015)

powered state. It is also found to vary by a factor  $\sim 1.6$  between two observations taken 6 months apart.

- We confirm the strong orbital X-ray and UV and optical modulations found by Bogdanov et al. (2014), Bassa et al. (2014) and dM14, respectively.

- The X-ray modulation amplitude is found to vary by a factor of  $\sim 2.7$  between the two epochs. The variability is consistent with X-rays originating at the intrabinary shock between the pulsar and donor star, which is eclipsed due to the companion orbital motion. Doppler boosting could be important to shape the X-ray modulation when the source brightens.

- The X-ray spectrum is non thermal ( $\Gamma=1.07$ ) and it is harder than that observed during the accretion-powered state and consistent with synchrotron emission from the intrabinary shock. The spectrum also softens at orbital minimum, a new feature seen only in one other redback so far. This could be due to a softer contribution of the outer regions of the shock and/or of the NS.

- The UV/optical/near-IR emission is modulated at the orbital period due to irradiation of the companion star. We infer a 5500 K temperature for the unheated hemisphere of the donor and a  $\sim 6500$  K temperature for the irradiated face. We also derive a binary inclination  $46^\circ \lesssim i \lesssim 65^\circ$  and a mass ratio  $0.11 \lesssim q \lesssim 0.26$ . For  $M_{\text{NS}} = 1.4 M_{\odot}$ , the donor mass is  $0.15 \lesssim M_2 \lesssim 0.36 M_{\odot}$ , confirming the redback nature of this binary.

- The UV/optical orbital modulation also changes in amplitude with time. The simultaneous UV and X-ray modulations behave opposite, the UV flux and amplitude being larger when the X-ray flux and amplitude are lower. This behaviour could be due to small changes in the mass flow rate from the donor star which affect the size of the intrabinary shock.

- The broad-band SED from radio to gamma-rays in the disc-free state is different from that observed during the LMXB state and composed by multiple contributions. The radio and GeV emissions are compatible with an origin from highly accelerated particles in the pulsar magnetosphere, while the X-rays are dominated by the intrabinary shock. The UV/optical and near-IR fluxes instead originate in the donor star. Whether the companion is heated by the intrabinary shock or by the pulsar spin-down power needs to be assessed with a higher energy coverage in the X-rays.

## ACKNOWLEDGMENTS

This work is based on observations obtained with *XMM-Newton*, an ESA science mission with instruments and contributions directly funded by ESA Member States, under programme 0729560. The authors wish to thank Dr. Norbert Schartel and the ESAC staff for their help in obtaining the XMM-Newton observation. The REM observations were obtained under programme DDT-REM:30901 and AOT-31:31002. The REM team is acknowledged for the support in the scheduling and data delivery. We acknowledge support from ASI/INAF I/037/12/0 and TMB from PRIN-INAF 2012-6. The Barcelona group acknowledges support from the grants AYA 2012-39303 and SGR 2014-1073. We are grateful to the anonymous referee, whose comments improved the clarity of this work.

## REFERENCES

- Alpar M., Cheng A., Ruderman M., Shaham J., 1982, Nature, 300, 728  
 Archibald A. et al., 2009, Science, 324  
 Arons J., Tavani M., 1993, ApJ, 403, 249  
 Backer D., Kulkarni S., Heiles C., Davies M., Goss M., 1982, Nature, 300, 615  
 Bassa C. G. et al., 2014, MNRAS, 441, 1825  
 Bégin S., 2006, Master's thesis, Faculty of Graduate Studies (Physics), The University of British Columbia  
 Bogdanov S., Archibald A., Hessels J., Kaspi V., Lorimer D., McLaughlin M., Ransom S., Stairs I., 2011, ApJ, 742, 97  
 Bogdanov S. et al., 2015, ApJ, 806, 148  
 Bogdanov S., Grindlay J. E., van den Berg M., 2005, ApJ, 630, 1029  
 Bogdanov S., Halpern J. P., 2015, ApJ, 803, L27  
 Bogdanov S., Patruno A., Archibald A. M., Bassa C., Hessels J. W. T., Janssen G. H., Stappers B. W., 2014, ApJ, 789, 40  
 Burderi L. et al., 2001, ApJ, 560, 71  
 Campana S., Stella L., Mereghetti S., Colpi M., Tavani M., Ricci D., Dal Fiume D., Belloni T., 1998, ApJ, 499, 65  
 Conconi P., Cuniffe R., D'Alessio F. e., 2004, in Moorwood F. M., Masanori I., eds, Proc. SPIE Vol. 5492, Ground-based Instrumentation for Astronomy. p. 1602  
 de Martino D. et al., 2013, A&A, 550, A89  
 de Martino D. et al., 2014, MNRAS, 444, 3004  
 de Martino D. et al., 2010, A&A, 515, 25  
 Hill A. et al., 2011, MNRAS, 415, 235  
 Huang R. H. H., Kong A. K. H., Takata J., Hui C. Y., Lin L. C. C., Cheng K. S., 2012, ApJ, 760, 92  
 Hui C. Y. et al., 2015, ApJ, 801, L27  
 Johnson T. J. et al., 2015, ApJ, 806, 91  
 Kennel C. F., Coroniti F. V., 1984, ApJ, 283, 694  
 Li J. et al., 2011, ApJ, 733, 89  
 Li K. L., Kong A. K. H., Takata J., Cheng K. S., Tam P. H. T., Hui C. Y., Jin R., 2014, ApJ, 797, 111  
 Masetti N. et al., 2006, A&A, 459, 21  
 Mason K. O. et al., 2001, A&A, 365, L36  
 Papitto A., de Martino D., Belloni T. M., Burgay M., Pellizzoni A., Possenti A., Torres D. F., 2015, MNRAS, 449, L26  
 Papitto A. et al., 2013, Nature, 501, 517  
 Papitto A., Torres D. F., 2015, ApJ, 807, 33  
 Papitto A., Torres D. F., Rea N., Tauris T. M., 2014, A&A, 566, A64  
 Patruno A. et al., 2014, ApJ, 781, L3  
 Patruno A., Watts A., 2012, in Belloni T., Mendez M., Zhang C., eds, Timing neutron stars: pulsations, oscillations and explosions. ASSL, in press (arXiv:0901.3516)  
 Possenti A., Cerutti R., Colpi M., Mereghetti S., 2002, A&A, 387, 993  
 Ritter H., Zhang Z.-Y., Kolb U., 2000, A&A, 360, 969  
 Roberts M. S. E., McLaughlin M. A., Gentile P. A., Ray P. S., Ransom S. M., Hessels J. W. T., 2015, ArXiv e-prints  
 Romani R. W., Filippenko A. V., Cenko S. B., 2015, ApJ, 804, 115  
 Romani R. W., Filippenko A. V., Silverman J. M., Cenko S. B., Greiner J., Rau A., Elliott J., Pletsch H. J., 2012,

- ApJ, 760, L36  
Roy J., Bhattacharyya B., Ray P., 2014, ATel, 5890  
Roy J. et al., 2015, ApJ, 800, L12  
Stappers B. et al., 2013, ATel, 5513  
Stappers B. W., Gaensler B. M., Kaspi V. M., van der Klis  
M., Lewin W. H. G., 2003, Science, 299, 1372  
Stella L., Campana S., Colpi M., Mereghetti S., Tavani M.,  
1994, ApJ, 432, 47  
Strüder L. et al., 2001, A&A, 365, L18  
Takata J. et al., 2014, ApJ, 785, 131  
Tendulkar S. P. et al., 2014, ApJ, 791, 77  
Turner M. J. L. et al., 2001, A&A, 365, L27  
Xing Y., Wang Z., 2014, ArXiv e-prints  
Zavlin V. E., 2006, ApJ, 638, 951  
Zerbi F., Chincarini G., Ghisellini G. e. a., 2004, in Moor-  
wood F. M., Masanori I., eds, Proc. SPIE Vol. 5492,  
Ground-based Instrumentation for Astronomy. p. 1590